

# Photoconductivity of biased graphene

Marcus Freitag<sup>\*</sup>, Tony Low, Fengnian Xia<sup>†</sup>, and Phaedon Avouris

IBM Thomas J. Watson Research Center, Yorktown Heights, New York 10598, USA

<sup>\*</sup> mfreitag@us.ibm.com

<sup>†</sup> fxia@us.ibm.com

## Abstract

Graphene is a promising candidate for optoelectronic applications such as photodetectors, terahertz imagers, and plasmonic devices. The origin of photoresponse in graphene junctions has been studied extensively and is attributed to either thermoelectric or photovoltaic effects. In addition, hot carrier transport and carrier multiplication are thought to play an important role. Here we report the intrinsic photoresponse in biased but otherwise homogeneous graphene. In this classic photoconductivity experiment, the thermoelectric effects are insignificant. Instead, the photovoltaic and a photo-induced bolometric effect dominate the photoresponse due to hot photocarrier generation and subsequent lattice heating through electron-phonon cooling channels respectively. The measured photocurrent displays polarity reversal as it alternates between these two mechanisms in a backgate voltage sweep. Our analysis yields elevated electron and phonon temperatures, with the former an order higher than the latter, confirming that hot electrons drive the photovoltaic response of homogeneous graphene near the Dirac point.

Optoelectronic properties of graphene have attracted substantial interest due to graphene's high carrier mobility, zero bandgap, and electron-hole symmetry.<sup>1</sup> Graphene can absorb light and turn it into a photocurrent over a wide range of the electromagnetic spectrum, from the UV to the visible and infrared regimes. A photocurrent response at graphene-metal contacts was reported by various groups including ours,<sup>2-5</sup> and in these early reports the origin of the photocurrent generation was attributed to the classical photovoltaic effect. The thermoelectric Seebeck effect, induced through photo-excited carriers, was first identified in single layer – bilayer graphene junctions experiments as the origin of photocurrent.<sup>6</sup> The technologically important photocurrent of graphene p-n junctions has been either described as photovoltaic<sup>5,7</sup> or thermoelectric<sup>8-10</sup> in nature. Both mechanisms may be enhanced by hot carriers<sup>11-15</sup> that persist after photoexcitation in graphene due to an electron-acoustic phonon decay bottleneck.<sup>9</sup> Electron-electron scattering on the other hand dominates the photocarrier energy relaxation, where the energetic photoexcited carriers multiply while decaying toward an elevated electronic temperature  $T_E$ .<sup>9,15</sup> The decoupling of electron and lattice temperatures in graphene may also explain how thermoelectric contributions can be compatible with the fast photoresponse on the order of 100GHz seen in modulated photocurrent measurements.<sup>16,17</sup> Due to the identical polarity of photovoltaic and thermoelectric currents in metal-graphene or graphene p-n junctions, it has been quite a challenge to identify the dominant photocurrent mechanism. However, the two effects show opposite polarity in the unipolar junction regimes  $p^+p$  and  $n^-n$ , which allowed the identification of the thermoelectric effect in the photocurrent of graphene on atomically flat boron-nitride dielectrics.<sup>10</sup> Very recently, a bolometric photoresponse was observed in gapped bilayer graphene.<sup>18</sup>

In this work, we investigate the origins of the photocurrent response in graphene by measuring the photoconductivity of the homogeneous graphene channel in a graphene field-effect transistor (FET) fabricated on Si/SiO<sub>2</sub>. In this simplest and yet unstudied configuration, the photocurrent polarities due to photovoltaic and thermoelectric effects are opposite, which allows us to directly determine the dominant photocurrent generation mechanism. In addition, the thermoelectric effect is an order of magnitude smaller than

the photovoltaic effect observed experimentally. Our results clearly reveal the importance of the photovoltaic effect particularly near the Dirac point, while a photo-induced bolometric effect dominates in the n-type and p-type doping regimes.

The graphene FETs in this work are biased at one contact with a moderate drain voltage on the order of  $V_D = -1V$ . The doping level in the graphene is controlled electrostatically via a global silicon backgate. While a chopped and focused laser beam at wavelength 690nm is scanned over the sample, we measure the AC photocurrent amplitude and phase, which are obtained by a lock-in amplifier referenced to the chopping frequency (Fig. 1a). Photocurrent images (Fig. 1c) show a uniform photocurrent within the interior of the graphene channel, exhibiting a photoresponse on the order of  $10^{-4} A/W$ . Contact effects, which have been discussed extensively for the zero bias case (Fig. 1b),<sup>2-6</sup> are limited to the immediate vicinity of the leads. Under applied bias, a small photocurrent ( $\sim 10\%$  of the observed value at graphene) is also observed when the laser beam is positioned a few microns away from the graphene, over the bare Si/SiO<sub>2</sub> substrate. The photocurrents from graphene and substrate exhibit opposite signs at  $V_G = 5V$ , as can be seen in the phase image. We show in the Suppl. Info. that the substrate-related photocurrent is due to a 2mV photovoltage generated at the Si/SiO<sub>2</sub> interface that is sensed by the graphene field-effect transistor. This “photo field-effect” switches sign when the Fermi level in the graphene is swept past the charge neutrality point. We can easily correct for its effect at the graphene position.

When photons are incident directly on the graphene channel, a true photocurrent from graphene ensues. This photocurrent switches sign twice when the Fermi level in the device is swept from p-type over to intrinsic and then to n-type (Fig. 2a). Figures 2b and 2c show the photocurrent in the center of the graphene as a function of gate voltage. Between gate voltages of  $V_G = 0V$  and  $V_G = 2.3V$ , which is close to the Dirac point, the photocurrent is positive and points in the direction of the DC current (from source to drain), while outside of this range, the photocurrent is negative. The largest photocurrent amplitude is reached at high electrostatic doping (positive or negative). Figure 3 shows the full gate and drain-voltage dependence of the AC photocurrent near the center of the

device. The six-fold pattern observed here is reminiscent of the situation observed in a dual-gated graphene p-n junction without source-drain bias, where a six-fold pattern as a function of the two independent gate voltages has been attributed to the thermoelectric Seebeck-effect.<sup>9,10</sup> In graphene under bias, the six fold pattern is composed of a two-fold sign change with gate voltage, and a single sign change with drain voltage. The well known tilt in the current-voltage characteristic (Fig. 3a) due to channel doping by the drain voltage, is also apparent in amplitude and phase of the AC photocurrent (Fig. 3b, c). The drain voltage dependence of the photocurrent is linear up to voltages on the order of a Volt, above which saturation sets in, especially at high doping (Fig. 3d and Suppl. Info.).

Several processes of photocurrent generation may play a role in biased graphene:

- (1) The thermoelectric Seebeck effect (TE): The laser spot produces a temperature gradient in the device, which together with a doping asymmetry generates a thermoelectric current. A typical experimental setup involves a p-n junction to produce the Seebeck effect.<sup>8-10</sup> While unbiased homogeneous graphene is not expected to produce a thermoelectric current, the presence of an applied drain voltage renders the electrochemical potential spatially variable, and a TE effect should ensue even in homogeneous graphene;
- (2) The photovoltaic effect (PV): Photo-excited electrons and holes are accelerated in opposite directions by the electric field. They produce a photocurrent either by reaching the contacts still hot, or by establishing a local photovoltage within the focal area that drives the photocurrent through the rest of the device;<sup>8</sup>
- (3) The bolometric effect (BOL): The incident electromagnetic radiation raises the local temperature of the graphene, which alters the resistance of the device, producing a change in DC current under bias.

Fig. 4 (a-c) summarizes the relative magnitude and signs of these effects in non-biased and biased graphene photodetectors. In the following we will discuss these effects in greater detail.

It is instructive to first review the basic TE effect in a p-n junction at zero bias.<sup>6,8,10</sup> Figure 4a illustrates the typical experimental situation, where the laser spot induces a temperature gradient and results in a net thermoelectric voltage across the

graphene due to the Seebeck effect. The generated photocurrent is proportional to  $(S_2 - S_1)dT/dx$ , where  $S_{1/2}$  is the Seebeck coefficient for the two sides of the junction. In the zero bias case, the sign of the thermoelectric photocurrent is the same as the photovoltaic effect, except for some unipolar junction regimes. This feature is most pronounced in very clean samples, leading to the six-fold sign change recently observed in graphene on boron nitride substrates.<sup>10</sup> When the graphene doping is homogeneous, the photocurrent will be zero. However, the uniform doping can be rendered asymmetric under an applied drain bias, such that the effective doping along the graphene channel changes gradually. This doping asymmetry and the associated Seebeck effect are more prominent at low doping. Typical energy band profiles are illustrated in Figs. 4b,c together with the sign of the various photocurrents relevant in our experiments. Near the charge neutrality point, the TE registers a photocurrent opposite in sign to both the experimentally measured photocurrent and the expected photovoltaic current. Since the Seebeck coefficient is related to the electrical conductivity  $\sigma$  through the Mott formula,  $S = -\frac{\pi^2 k_b^2 T}{3e} \frac{1}{\sigma} \frac{d\sigma}{d\varepsilon}$ , application of the thermoelectric theory yields us an estimate of a TE photocurrent of approximately 4nA near the Dirac point (see Suppl. Info.), opposite and an order smaller than that observed in experiment. Away from  $V_G = V_{\text{Dirac}}$ , the TE effect is expected to be even less important because the electrochemical potential asymmetry is reduced with increasing Fermi level.

Next we consider the bolometric response of the graphene photodetector, which can only be observed in biased devices, and was therefore absent in previous short-circuit measurements on graphene contacts or junctions.<sup>2-10</sup> The bolometric effect can be determined by a measurement of the temperature dependence of the transport current. Figure 5a shows the change in transport current  $\Delta I$  compared to its room temperature value when cooling down in the cryostat. From this we can extract the gate-voltage dependent bolometric coefficient  $\beta(V_G) = \Delta I(V_G)/\Delta T(V_G)$  (Fig. 5b, red curve), which describes the sensitivity of the transport current to changes in temperature around room temperature.<sup>19-21</sup> A similar measurement around our lowest temperature of  $T_0 = 205\text{K}$

yields the other (blue) curve for the temperature coefficient in Fig. 5b. The negative values of  $\beta(V_G)$  in single-layer graphene are due to electron-acoustic phonon scattering and electron-remote phonon scattering of surface polar phonons in the SiO<sub>2</sub> underlayer, which both are enhanced at elevated temperatures.<sup>19</sup> For comparison, Fig. 5c shows the experimental photocurrents at room temperature and  $T_0=205\text{K}$ . The similar shapes of the curves in Figs. 5b and 5c are striking. In particular, both the bolometric coefficient and the photocurrent are largest (and negative) at high doping and the electron-hole asymmetry of the temperature coefficient is reproduced in the photocurrent measurement. While the bolometric effect can explain these general features of the gate-voltage dependence of the photocurrent, it cannot explain the positive photocurrent in the direction of the DC current under low doping.

The photovoltaic effect (PV) is the only known mechanism that is consistent with the positive photoresponse near the Dirac point seen experimentally. Under light excitation, the hot carriers with separated electron and hole chemical potentials are formed on a timescale of the order of 100 fs, followed by a slow pico-second carrier recombination and cooling.<sup>11-16</sup> At steady state, the photo-induced carrier density  $n_{e/h}^*$  depends on its non-equilibrium carrier temperature  $T_e$  and the chemical potential and has to be determined by imposing charge conservation i.e.  $n_e^* = n_h^*$ . In addition,  $T_e$  has its maximum at the focal spot and is proportional to  $\dot{Q}L/\kappa_0$  where  $\dot{Q}$  is the laser power and  $\kappa_0$  is the electronic thermal conductivity, related to the electronic conductivity through the Wiedemann-Franz relation. Making use of the above facts allows us to compute the gate dependent photo-induced carrier densities  $n_{e/h}^*(V_G)$  (Suppl. Info). The photovoltaic current can then be estimated from  $qn^*\mu\xi$ , where  $\xi$  is the electric field and  $\mu \approx 2700\text{cm}^2/\text{Vs}$  our device's carrier mobility. In general, the non-equilibrium  $n_{e/h}^*$  decrease with increasing equilibrium doping, consistent with the fact that electron-electron scattering which serves as efficient means towards carrier equilibration increases with doping. Hence, the modeled photovoltaic current as shown in Fig. 5c decreases gradually with increasing bias away from the charge neutrality point. Near the Dirac

point, the elevated electron temperatures are  $T_E = T_e - T_0 \approx 8\text{K}$  and  $12\text{K}$  at initial temperatures  $T_0 = 300\text{K}$  and  $200\text{K}$  respectively as shown in Fig. 5d, which also decrease with increasing equilibrium doping.

Next, we subtract the estimated photovoltaic current component from our experimentally measured photocurrent, to obtain the purely bolometric contribution  $I_{\text{BOL}}$ . The elevated lattice temperature  $T_L = T_{\text{ph}} - T_0$  can then be determined from the ratio  $I_{\text{BOL}}/\beta$ , where  $\beta$  is the experimentally determined bolometric coefficient (Fig. 5b) discussed earlier. As shown in Fig. 5d,  $T_L$  is of the order of a Kelvin and is weakly dependent on doping. Both  $T_L$  and  $T_E$  are enhanced at lower temperatures due to less efficient cooling. Although electron-electron interactions result in an energy equilibration of the electronic system, they do not lead to a net energy loss. The dominant energy loss pathways are due to phonons. Intrinsic energy loss channels due to acoustic/optical phonons are known to be inefficient energy loss pathways and have only a power density  $Q_l \approx 10^2 - 10^4 \text{ W/m}^2$  for  $T_E - T_L = 10\text{K}$  (Suppl. Info.).<sup>13,22</sup> With a typical graphene-substrate thermal resistance of  $r_{sg} \approx 10^{-7} \text{ Km}^2/\text{W}$ ,<sup>23,24</sup> our measured lattice temperature suggests a lattice heating power density of the order of  $Q_l = T_L/r_{sg} \approx 10^7 \text{ W/m}^2$  or somewhat lower, because of the uncertainty in the temperature at the Si/SiO<sub>2</sub> interface after photoexcitation. The inferred larger power density in experiments may indicate the presence of more efficient energy loss pathways in graphene devices. Electron-remote phonon scattering of surface polar phonons in the SiO<sub>2</sub> underlayer,<sup>19,25-27</sup> and extrinsically enhanced phonon-scattering processes mediated by ionized impurity and random strain induced gauge fields<sup>28</sup> may provide these additional decay pathways. More systematic studies in this direction are needed to clearly identify the energy dissipation mechanisms in graphene.

In conclusion, our measurement and theory of the intrinsic photoconductivity of biased graphene show that both bolometric and photovoltaic effects are relevant in its photoresponse. The polarity and magnitude of the photocurrent can be modulated by

electrostatic doping, which upon examination allows us to probe the non-equilibrium hot carrier and phonon characteristics. Our studies therefore open up the possibility of engineering the hot carrier photoresponse, which plays an essential role in applications such as bolometers, calorimeters and photodetectors.

## Methods

Graphene field-effect transistors are fabricated by mechanical exfoliation from graphite. E-beam lithography and evaporation of 15nm/70nm of Ti/Au are used for the contacts. A second e-beam lithography step and plasma etching defines rectangular graphene sheets with length and width of 6 $\mu$ m and 1 $\mu$ m. Single-layer graphene is identified by its optical contrast on the 90nm SiO<sub>2</sub> dielectric. We use a highly doped (n-type) silicon substrate to avoid an excessive photo field-effect, which dominates measurements on samples fabricated on lightly doped silicon. The as-prepared samples behave p-type. To render them intrinsic, enhance mobility, and reduce hysteresis, the samples are evacuated for a few days prior to the measurements and subjected to a combination of current annealing and laser scanning with a green laser for an hour. After this treatment, the Dirac point is near  $V_G=0V$ . AC photoconductivity measurements are performed with a Ti/Sapphire infrared laser at around  $\lambda = 690nm$ . The laser spot diameter on the sample is about  $d \approx 700nm$ . Incident laser power values are given in the Figure captions. Considering the electric-field enhancement due to the gate stack, we estimate that 2.5% of the incident light is absorbed in the graphene. The photocurrent amplitudes reported in this paper are peak-to-peak values throughout. We confirm that the chopping frequency  $f = 1.1KHz$  is not too large by comparing our AC photocurrent results with equivalent DC measurements, which have much worse signal/noise, but agree with the photocurrent phase reported in this paper. The photocurrent measurements are performed in an optical dewar with vacuum on the order of  $10^{-5}$ - $10^{-6}$  Torr, eliminating the effects of photodesorption of oxygen,<sup>29</sup> and allowing us to measure the temperature-dependence.



## References:

- 1 Bonaccorso, F., Sun, Z., Hasan, T. & Ferrari, A. C. Graphene photonics and optoelectronics. *Nat Photon* **4**, 611-622 (2010).
- 2 Lee, E. J. H., Balasubramanian, K., Weitz, R. T., Burghard, M. & Kern, K. Contact and edge effects in graphene devices. *Nat Nano* **3**, 486-490 (2008).
- 3 Mueller, T., Xia, F., Freitag, M., Tsang, J. & Avouris, P. Role of contacts in graphene transistors: A scanning photocurrent study. *Physical Review B* **79**, 245430 (2009).
- 4 Xia, F. *et al.* Photocurrent Imaging and Efficient Photon Detection in a Graphene Transistor. *Nano Letters* **9**, 1039-1044 (2009).
- 5 Peters, E. C., Lee, E. J., Burghard, M. & Kern, K. Gate dependent photocurrents at a graphene p-n junction. *Appl. Phys. Lett.* **97**, 193102 (2010).
- 6 Xu, X., Gabor, N. M., Alden, J. S., van der Zande, A. M. & McEuen, P. L. Photo-Thermoelectric Effect at a Graphene Interface Junction. *Nano Letters* **10**, 562-566 (2009).
- 7 Rao, G., Freitag, M., Chiu, H.-Y., Sundaram, R. S. & Avouris, P. Raman and Photocurrent Imaging of Electrical Stress-Induced p-n Junctions in Graphene. *ACS Nano* **5**, 5848-5854 (2011).
- 8 Lemme, M. C. *et al.* Gate-Activated Photoresponse in a Graphene p-n Junction. *Nano Letters* **11**, 4134-4137 (2011).
- 9 Song, J. C. W., Rudner, M. S., Marcus, C. M. & Levitov, L. S. Hot Carrier Transport and Photocurrent Response in Graphene. *arXiv:1105.1142v2 [cond-mat.mes-hall]* (2011).
- 10 Gabor, N. M. *et al.* Hot Carrier-Assisted Intrinsic Photoresponse in Graphene. *Science* (2011).
- 11 George, P. A. *et al.* Ultrafast Optical-Pump Terahertz-Probe Spectroscopy of the Carrier Relaxation and Recombination Dynamics in Epitaxial Graphene. *Nano Letters* **8**, 4248-4251 (2008).

- 12 Sun, D. *et al.* Ultrafast Relaxation of Excited Dirac Fermions in Epitaxial Graphene Using Optical Differential Transmission Spectroscopy. *Physical Review Letters* **101**, 157402 (2008).
- 13 Bistritzer, R. & MacDonald, A. H. Electronic Cooling in Graphene. *Physical Review Letters* **102**, 206410 (2009).
- 14 Strait, J. H. *et al.* Very Slow Cooling Dynamics of Photoexcited Carriers in Graphene Observed by Optical-Pump Terahertz-Probe Spectroscopy. *Nano Letters* (2011).
- 15 Kim, R., Perebeinos, V. & Avouris, P. Relaxation of optically excited carriers in graphene. *Physical Review B* **84**, 075449 (2011).
- 16 Urich, A., Unterrainer, K. & Mueller, T. Intrinsic Response Time of Graphene Photodetectors. *Nano Letters* **11**, 2804-2808 (2011).
- 17 Xia, F., Mueller, T., Lin, Y.-m., Valdes-Garcia, A. & Avouris, P. Ultrafast graphene photodetector. *Nat Nano* **4**, 839-843 (2009).
- 18 Yan, J. *et al.* Dual-gated bilayer graphene hot electron bolometer. *arXiv:1111.1202v1 [cond-mat.mes-hall]* (2011).
- 19 Chen, J.-H., Jang, C., Xiao, S., Ishigami, M. & Fuhrer, M. S. Intrinsic and extrinsic performance limits of graphene devices on SiO<sub>2</sub>. *Nat Nano* **3**, 206-209 (2008).
- 20 Zhu, W., Perebeinos, V., Freitag, M. & Avouris, P. Carrier scattering, mobilities, and electrostatic potential in monolayer, bilayer, and trilayer graphene. *Physical Review B* **80**, 235402 (2009).
- 21 Efetov, D. K. & Kim, P. Controlling Electron-Phonon Interactions in Graphene at Ultrahigh Carrier Densities. *Physical Review Letters* **105**, 256805 (2010).
- 22 Tse, W.-K. & Das Sarma, S. Energy relaxation of hot Dirac fermions in graphene. *Physical Review B* **79**, 235406 (2009).
- 23 Freitag, M. *et al.* Energy Dissipation in Graphene Field-Effect Transistors. *Nano Letters* **9**, 1883-1888, doi:10.1021/nl803883h (2009).
- 24 Koh, Y. K., Bae, M.-H., Cahill, D. G. & Pop, E. Heat Conduction across Monolayer and Few-Layer Graphenes. *Nano Letters* **10**, 4363-4368, doi:10.1021/nl101790k (2010).

- 25 Meric, I. *et al.* Current saturation in zero-bandgap, top-gated graphene field-effect transistors. *Nat Nano* **3**, 654-659 (2008).
- 26 Perebeinos, V., Rotkin, S. V., Petrov, A. G. & Avouris, P. The Effects of Substrate Phonon Mode Scattering on Transport in Carbon Nanotubes. *Nano Letters* **9**, 312-316, doi:10.1021/nl8030086 (2008).
- 27 Rotkin, S. V., Perebeinos, V., Petrov, A. G. & Avouris, P. An Essential Mechanism of Heat Dissipation in Carbon Nanotube Electronics. *Nano Letters* **9**, 1850-1855, doi:10.1021/nl803835z (2009).
- 28 Song, J. C. W., Reizer, M. Y. & Levitov, L. S. Supercollisions and the Bottleneck for Electron-Lattice Cooling in Graphene. *arXiv:1111.4678v1 [cond-mat.mes-hall]* (2011).
- 29 Shi, Y., Fang, W., Zhang, K., Zhang, W. & Li, L.-J. Photoelectrical Response in Single-Layer Graphene Transistors. *Small* **5**, 2005-2011 (2009).

**Figure 1**

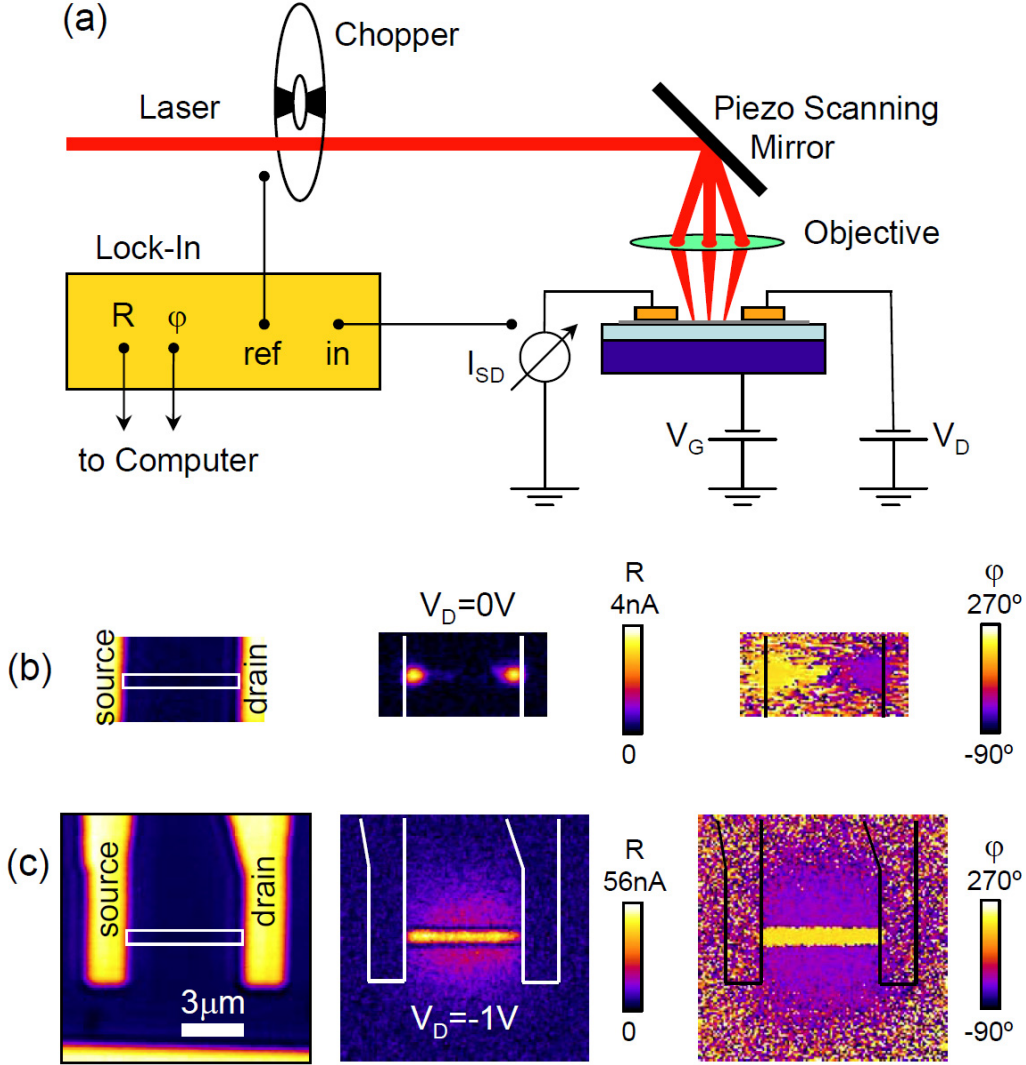


**Figure 1: AC photoconductivity of graphene with and without bias.** (a) Schematic of the photoconductivity measurement setup with  $\lambda = 690\text{nm}$  laser wavelength,  $P = 220\mu\text{W}$  laser power,  $d \approx 700\text{nm}$  spot diameter, and  $f = 1.1\text{KHz}$  chopping frequency. (b) AC photocurrent at  $V_D = 0\text{V}$  drain bias (short-circuit photocurrent) and  $V_G = 5\text{V}$  gate bias (n-type regime). The laser-scanning image (left) shows source and drain electrodes. The outline of the graphene sheet is indicated. Middle: Amplitude (R) of the photocurrent. Right: Phase ( $\phi$ ) of the photocurrent. A localized photocurrent is generated close to the contacts. The phase at source and drain contacts are  $\phi \approx 180^\circ$  (corresponding

to negative  $I_{\text{ph}}$ ) and  $\varphi \approx 0^\circ$  (positive  $I_{\text{ph}}$ ) respectively. **(c)** AC photocurrent under a drain bias of  $V_{\text{D}}=-1\text{V}$  and gate voltage  $V_{\text{G}}=5\text{V}$ . Laser scanning, amplitude, and phase images are shown. The entire graphene channel is producing a photocurrent under applied bias, and the photocurrent is uniform in both amplitude ( $R \approx 46\text{nA}$ ) and phase ( $\varphi \approx 180^\circ$ ) throughout the channel except for the contact regions. The small photocurrent generated next to the graphene channel is in response to a photovoltage at the Si/SiO<sub>2</sub> interface that couples capacitively to the graphene field-effect transistor.

**Figure 2**

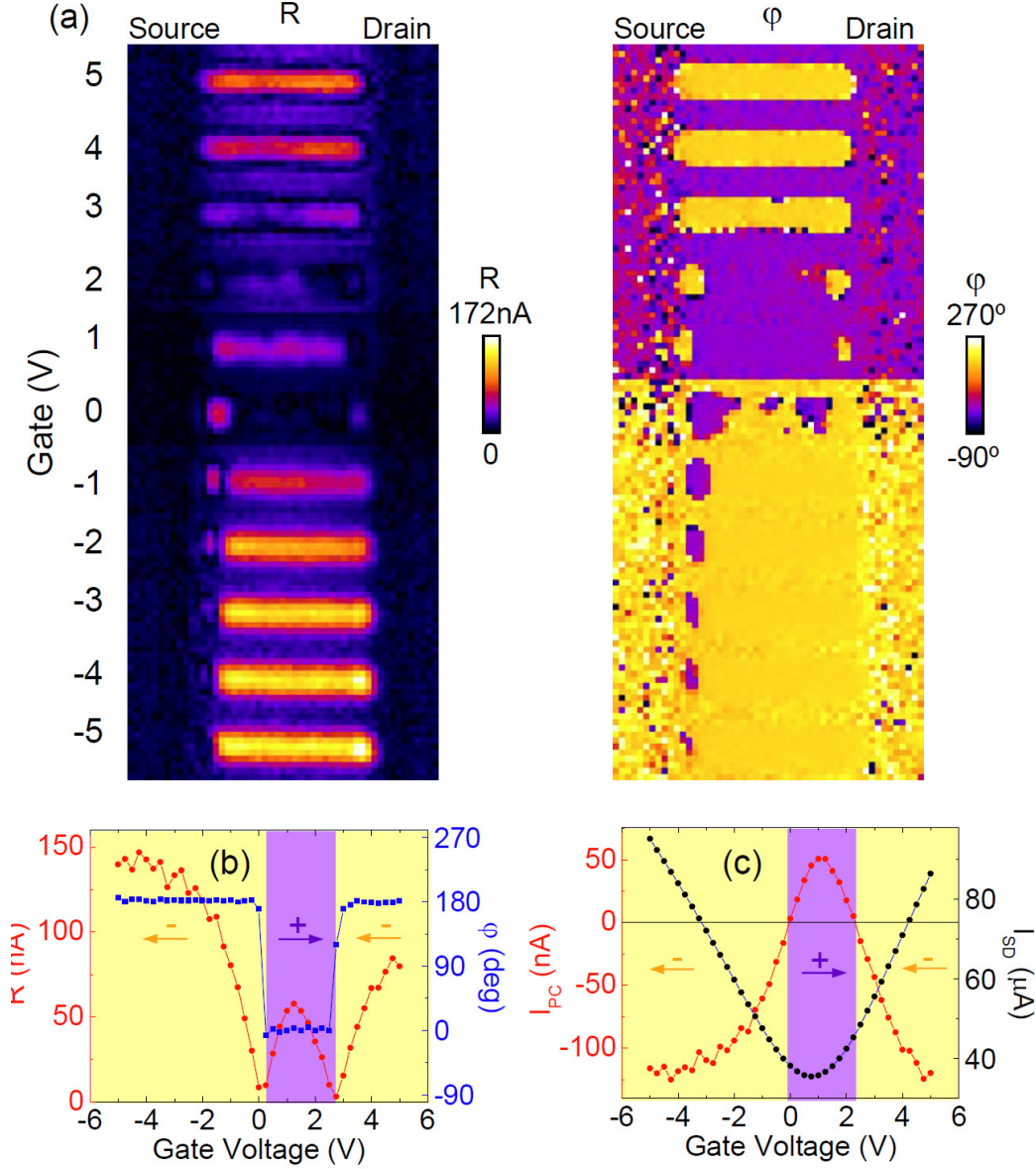


**Figure 2: AC Photocurrent as a function of gate voltage.** (a) Spatial images of the photocurrent amplitude and phase as a function of gate voltage. (Drain voltage  $V_D = -1V$ ; laser power  $P = 370\mu W$ ). The photocurrent in the graphene channel switches sign twice from negative ( $\phi \approx 180^\circ$ ) to positive ( $\phi \approx 0^\circ$ ) and back to negative ( $\phi \approx 180^\circ$ ). (b) Photocurrent amplitude (red) and phase (blue) in the center of the graphene channel as a function of gate voltage. The sign of the photocurrent is indicated.

For comparison, the DC current has positive sign for  $V_D = -1V$ . **(c)** Photocurrent (red) corrected for the photo field-effect (Suppl. Info.) and source-drain current (black) as a function of gate voltage.

**Figure 3**

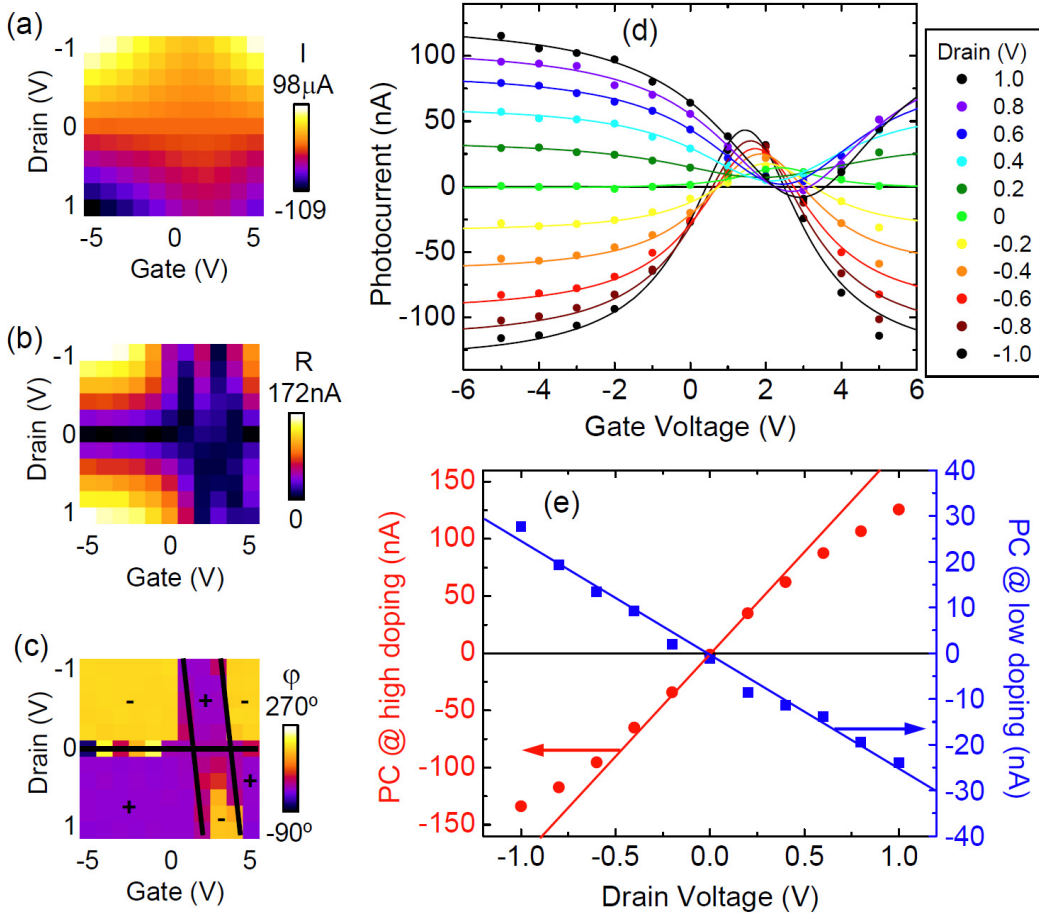


**Figure 3: Gate and drain voltage dependence of the photocurrent.** (a) DC current, (b) photocurrent amplitude, and (c) photocurrent phase, as a function of gate and drain voltages. Solid lines indicate the modeled sign change. (d) Gate voltage characteristics of the photocurrent for different drain voltages, corrected for the photo field-effect. Solid lines are Lorentzian fits to the data. A 16nA photocurrent near the Dirac point at  $V_D=0\text{V}$  is due to residual doping. (e) Peak bias-induced photocurrents at high and low doping as a function of drain voltage. (Solid lines are a guide to the eye.) The photocurrent at high doping is due to the Bolometric effect, while the photocurrent at low doping is due to the Photovoltaic effect.



**Figure 4**

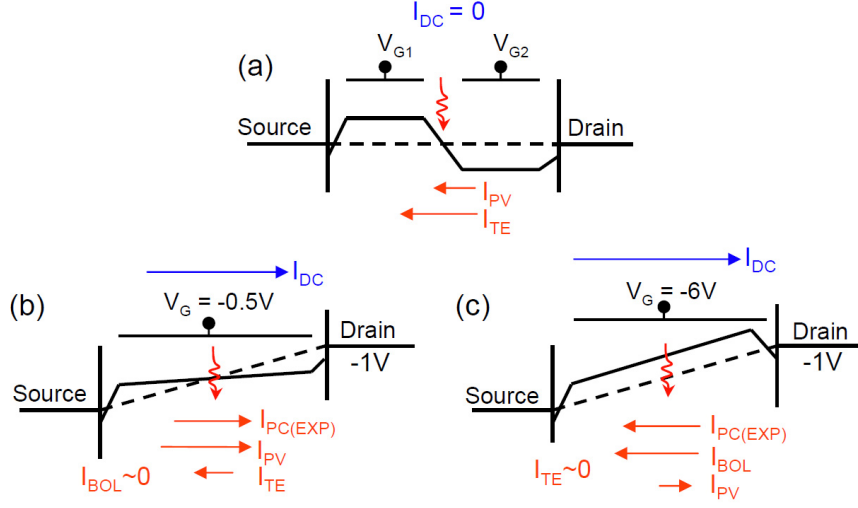


**Figure 4: Thermoelectric, Bolometric, and Photovoltaic components of the graphene photocurrent.** (a) Energy band diagram of a graphene p-n junction used in typical photocurrent experiments, with laser incident at the junction interface. The DC current and thus the BOL current are zero. TE and PV components point in the same direction. (b, c) Energy band diagrams for our experiments, where a uniform graphene channel is subjected to a finite source-drain bias  $V_D$ , under small and large electrostatic doping conditions respectively. The directions of the photocurrent components are indicated. At low electrostatic doping the PV effect dominates, while at high electrostatic doping the BOL effect overshadows both PV and TE effects.

**Figure 5**

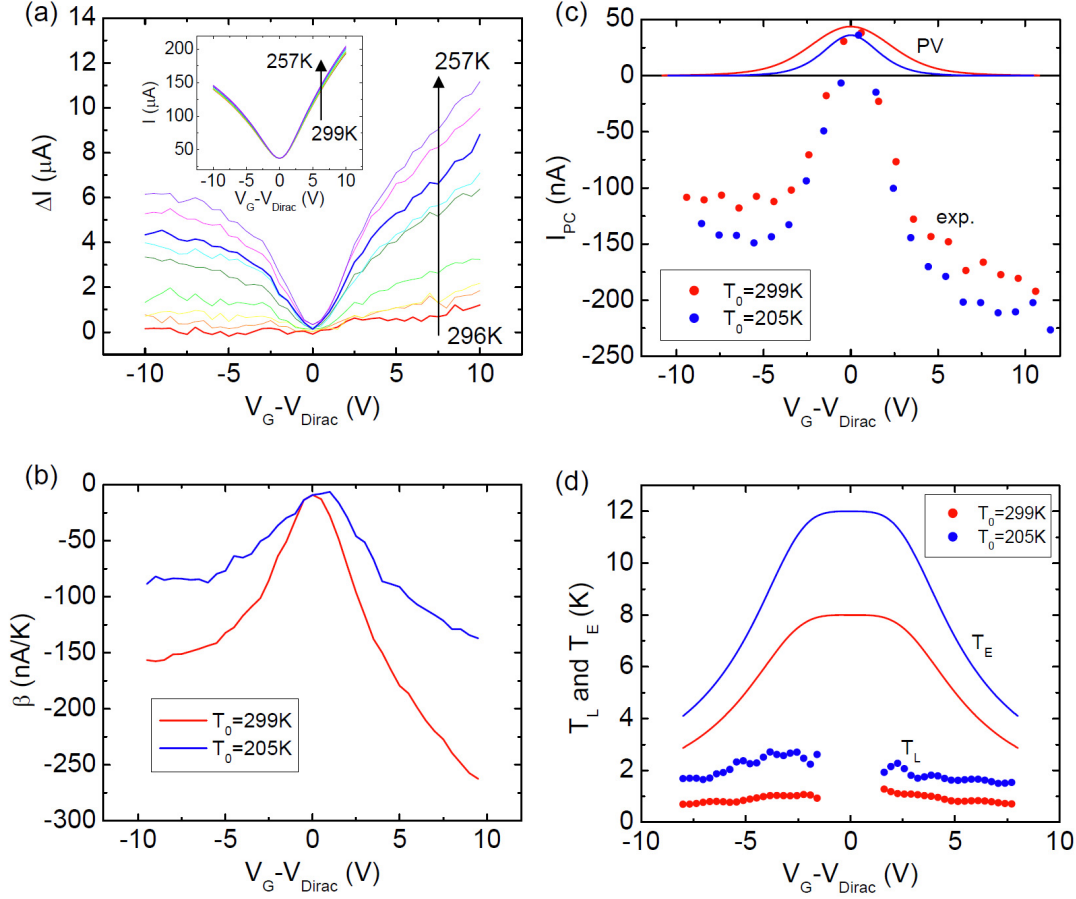


**Figure 5: Magnitude of BOL and PV effects and determination of the hot electron and lattice temperatures.** (a) Temperature-dependent change in current from its room temperature ( $T_0=299\text{K}$ ) value, as a function of gate voltage. **Inset:** Gate-voltage characteristic as a function of temperature when cooling down from room temperature. (b) Bolometric coefficient  $\beta(V_G) = \Delta I(V_G) / \Delta T(V_G)$  of the transport current as a function of gate voltage at two different ambient temperatures  $T_0$  as indicated. (c) Experimental photocurrent (corrected for the photo field-effect) and modeled photovoltage component of the photocurrent. The PV component is important only near charge neutrality where it determines the sign of the overall photocurrent. Away from the Dirac point, the bolometric effect (b) dominates. (d) Electron ( $T_E$ ) and lattice ( $T_L$ ) temperatures extracted from the data as detailed in the text.

**Supplementary Information:**  
**Photoconductivity of biased graphene**

Marcus Freitag, Tony Low, Fengnian Xia, and Phaedon Avouris

*IBM T.J. Watson Research Center,*

*Yorktown Heights, NY 10598, USA*

(Dated: February 27, 2012)

## I. EXTRACTING AND CORRECTING FOR THE PHOTO FIELD-EFFECT

We are interested in the photocurrent that is generated by photons absorbed in the active channel of the graphene photodetector. These photons produce electron-hole pairs in the graphene, which rapidly decay into a cloud of hot electrons and holes, leading to photocurrents due to the photovoltaic, thermoelectric, and bolometric effects. In addition, there exists a photocurrent contribution that is extrinsic to the graphene photodetector, and which we would like to correct for. This contribution is due to light absorbed in the Silicon substrate close to the Si/SiO<sub>2</sub> interface, producing a photovoltage at the interface, which is picked up by the gate-sensitive graphene field-effect transistor as a change in source-drain current. It should be possible to avoid this “photo field-effect”, by using metallic gates, but as we show below, it is also easy to correct for the effect because the intrinsic and extrinsic photocurrent contributions can be spatially decomposed.

Due to a workfunction mismatch between Silicon and Silica, the conduction and valence bands in Silicon bend at the interface. For n-type doping of the Silicon substrate as in our case, the bands in Silicon bend upward, which leads to a triangular potential well for holes at the interface [1]. Photo-generated holes diffuse toward the interface, while electrons are repelled from the interface. This leads to an additional positive voltage on the interface, which acts just like an applied positive gate voltage would in the graphene field-effect transistor, altering the source-drain current. Since the transconductance of a graphene field-effect transistor switches sign at the Dirac point, the photo field-effect also switches sign at the Dirac point ( $V_{CNP} \approx 1\text{ V}$  in Fig. S1a). This is in contrast to the intrinsic photocurrent, which switches sign twice, as discussed in the main text.

The magnitude and spatial extend of the photo field-effect depends on the substrate chemical doping. For intrinsic or lightly doped silicon, the carrier lifetime is long, and the magnitude and spatial extend can be large (centimeters). For heavily doped Silicon, as in our case, the lifetime is shorter, but we still measure a photo field-effect, as can be seen from Fig. S1a, where the photocurrent is plotted as a function of gate voltage and position perpendicular to the graphene channel. The intrinsic photocurrent components decay rapidly once the laser spot moves away from the graphene, but the photo field-effect remains

up to a distance of several microns. This behavior allows us to estimate the magnitude of the photo field-effect at the position of the graphene by considering the photocurrent that is generated away from the graphene and fitting it spatially to Lorentzians as exemplified in Fig. S1b. Figure S1e shows the values of the extracted photo field-effect at the center of the graphene as a function of gate voltage. As expected, the curve is proportional to the transconductance  $g_m$  extracted from the  $I - V_G$  characteristic. The proportionality factor is  $2 \text{ nA}/\mu\text{S}$  at a laser power of  $370 \mu\text{W}$ . This means that a photovoltage of  $2 \text{ mV}$  is generated at the Si/SiO<sub>2</sub> interface. We can now subtract the photo field-effect component from the total photocurrent and obtain the intrinsic photocurrent in Figs. S1c and S1f. This latter result is used as the basis for our model on the photovoltaic and bolometric components of the intrinsic photocurrent.

## II. SPATIAL DISTRIBUTION OF THE AC PHOTOCURRENT AND PHOTOCURRENT SATURATION AT HIGH BIAS

The spatial distribution of the photocurrent in biased graphene along the channel direction is shown in Fig. S2 as a function of gate voltage for different drain voltages. At zero drain voltage, the well-known contact effect is present, where regions close to the metallic leads become photoactive because of band-bending there. Both the photovoltaic effect and the Seebeck effect likely play a role in this regime. The contact effect is strongest with the graphene channel electrostatic doping opposite to the metal-induced doping of the graphene beneath the leads, which produces two back-to-back p-n junctions. In our case the metal dopes the graphene n-type and p-n junctions exist for negative gate voltages. These junctions move further into the channel for gate voltages that approach the flat-band voltage at  $V_G=2\text{V}$ . At more positive gate voltages, no p-n junctions exist, and the photocurrent from the contact regions is smaller and is generated right at the contacts.

Once a drain bias in excess of about  $V_D=0.5\text{V}$  is applied, the bias-induced photocurrent, which is the topic of this paper, dominates. The high spatial uniformity of this photocurrent is apparent at  $V_D=-1\text{V}$ , where the middle  $4\mu\text{m}$  of the  $6\mu\text{m}$  long graphene shows essentially the same photocurrent and gate-voltage dependence. Contact effects are limited to a  $1\mu\text{m}$  area next to the metal leads. There is a slight tilt in the gate-voltage characteristic due to

drain-voltage induced doping of the channel interior, which affects the right (drain) side of the device more than on the left, and which shifts the photocurrent pattern down by 1V at the drain and half of that (0.5V) in the center of the device. This tilt becomes stronger at  $V_D=-2V$  and  $-3V$  as expected. In fact, one can use these photocurrent measurements to determine the Dirac point inside the biased graphene channel as a function of x-position.

The saturating behavior of the bolometric component of the photocurrent is already becoming apparent below  $V_D=-1V$  (see main text Fig. 3e). The color-scale bars in Fig. S2 show that at higher drain voltages both the BOL and PV components indeed saturate. Once the electron temperature is elevated due to the bias, additional photogenerated carriers will not be able to increase the electron temperature as much as before, because the photocarrier lifetime will be reduced if the electron distribution is already hot. The high bias thus limits both BOL and PV components of the AC photocurrent.

### III. DEVICE MODELING

We consider back-gated ( $V_G$ ) graphene devices, where the left contact is grounded i.e.  $V_L = 0$  and  $V_R$  allowed to vary. Our model considers the operating regime where the bias current  $I_{dc}$  induced by  $V_R$  is still in the linear regime. The electrochemical potential  $\mu$  in the graphene channel ( $-\frac{L}{2} < x < \frac{L}{2}$ ) is simply,

$$\mu(x) = \frac{eV_R}{L}x - \frac{eV_R}{2} \quad (1)$$

The electrical potential energy  $\Phi(x)$  (or Dirac point energy) is given by,

$$\begin{aligned} \Phi(x) &= \frac{\beta_R - \beta_L}{L}x + \frac{\beta_R + \beta_L}{2} + \mu(x) \\ \beta_{L/R} &= -\text{sign}(V_G - V_{L/R}) \times \hbar v_f \sqrt{\frac{1}{e} \pi C_B |V_G - V_{L/R}|} \end{aligned} \quad (2)$$

To keep the analytics tractable, we fit the electrical conductivity phenomenologically for electron-hole puddles,

$$\sigma(\epsilon) = \frac{\sigma_{min}}{\Delta^2} \sqrt{\epsilon^4 + \Delta^4} \quad (3)$$

where  $\epsilon$  is defined to be  $\epsilon = \mu - \Phi$ .  $\sigma_{min}$  is the minimum conductivity and  $\Delta$  represents the neutrality region energy width. Both can be simply extracted from the experiments, through  $\langle \sigma \rangle = \frac{1}{L} \int \sigma(\epsilon) dx$ . In our experiments, device physical dimensions are  $W \times L = 1 \times 6 \mu m$

and  $t_{ox} = 90$  nm. The experimentally measured graphene electrical conductivity is fitted to Eq. 3, with best fit values of  $\sigma_{min} = 2.3 \times 10^{-4}$  S and  $\Delta = 75$  meV. In our experiment, the extracted effective mobility around the neutrality point is  $\mu = 0.27$  m<sup>2</sup>/Vs.

#### IV. THERMOELECTRIC CURRENT MODELING

The Seebeck coefficient is computed using the Mott formula[2],

$$\mathcal{S}_g = -\frac{\pi^2 k_B^2 T}{3e} \frac{1}{\sigma} \frac{d\sigma}{d\epsilon} = -\frac{\pi^2 k_B^2 T}{3e} \frac{2\epsilon^3}{\epsilon^4 + \Delta^4} \quad (4)$$

The second equality makes use of Eq. 3. Hence,  $\mathcal{S}_g$  for each location in  $x$  can be computed. The photocurrent density (Am<sup>-1</sup>) generated by the thermoelectric effect can be computed through,

$$J_{TE} = -\frac{\langle \sigma \rangle}{L} \int_{-\frac{L}{2}}^{\frac{L}{2}} \mathcal{S}_g(x) \frac{d\mathcal{T}_{e/h}}{dx} dx \quad (5)$$

As mentioned in the main manuscript, the uniform channel doping can be rendered asymmetric under an applied drain bias, such that the effective doping along graphene changes gradually across the two contacts. This spatial variation in doping is described by  $\Phi(x) - \mu(x)$  (see Eq. 2), from which the resulting Seebeck coefficient can be computed from Eq. 4.

Consider photo-excitation in the middle of the graphene channel. A simplified model for the hot electron/hole temperature profiles due to photo-excitation suffice [3]:

$$\mathcal{T}_{e/h}(x) = \frac{\dot{Q}L}{\kappa_0} \Lambda(x) + \mathcal{T}_0 \quad (6)$$

where  $\mathcal{T}_0$  is the ambient temperature,  $\dot{Q}$  is the absorbed laser power,  $L$  the device length and  $\kappa_0$  is the electronic thermal conductivity, where  $\kappa_0$  and  $\sigma$  are related through the Wiedemann-Franz relation.  $\Lambda(x)$  is a triangular function, with maximum at the middle of the channel i.e.  $x = 0$  and zero at  $x = \pm \frac{1}{2}L$ . As discussed in Sec. V,  $\mathcal{T}_{e/h}(x)$  has a maximum temperature of 8 K in the middle of the channel. The thermoelectric current calculated from Eq. 5 yields  $I_{TE} \approx 4$  nA at  $V_R = 1$  V and when graphene channel is biased near charge neutrality. This thermoelectric effect is an order smaller than the corresponding photocurrent observed in experiment and also has an opposite sign.

## V. PHOTOVOLTAIC CURRENT MODELING

As argued in the main manuscript, the observed photocurrent of  $I_{PV} \approx 40$  nA in graphene when biased near the charge neutrality point (i.e.  $V_G = 0$ ) is due to a photovoltaic contribution. The photovoltaic current can be modeled by,

$$J_{PV} = \sigma^* \xi = \frac{\sigma^*}{L} (\beta_R - \beta_L - eV_R) \quad (7)$$

where  $\sigma^*$  is the photoexcited conductivity. With an applied drain bias of  $V_R = -1$  V and source  $V_L = 0$  V, the calculated channel electric field (using Eq. 2) when the device is biased near the charge neutrality point is  $\xi = 1.53 \times 10^5$  V/m. This yields us  $\sigma^* = 2.6 \times 10^{-7}$  S. Since  $\sigma^*$  can be expressed as  $\sigma^* \approx qn^*\mu^*$ , where  $n^*$  is the photo-induced carrier density and  $\mu^*$  the effective mobility of these excited carriers, where we assumed  $\mu^* \approx \mu = 0.27$  m<sup>2</sup>/Vs, where  $\mu$  is inferred from experiments. We obtain  $n^* = 6 \times 10^{12}$  m<sup>-2</sup> at  $V_G = 0$ .

The photo-induced electron and hole densities at the laser spot are estimated to be  $n_e^* = n_h^* \approx g_f n^*/2$ , where  $g_f = WL/a_{spot} \approx 16$  is a geometrical scaling factor with  $a_{spot}$  being the focal area. Hence  $n_{e/h}^* \approx 5 \times 10^{13}$  m<sup>-2</sup> at  $V_G = 0$ .  $n_e^*$  and  $n_h^*$  as function of  $V_G$  can be modeled with,

$$\begin{aligned} n_e^* &= \int_0^\infty D(\epsilon) f(\epsilon, \mathcal{T}_e^1, \mu_e^1) d\epsilon - \int_0^\infty D(\epsilon) f(\epsilon, \mathcal{T}^0, \mu^0) d\epsilon \\ n_h^* &= \int_{-\infty}^0 D(\epsilon) [1 - f(\epsilon, \mathcal{T}_h^1, \mu_h^1)] d\epsilon - \int_{-\infty}^0 D(\epsilon) [1 - f(\epsilon, \mathcal{T}^0, \mu^0)] d\epsilon \end{aligned} \quad (8)$$

and

$$C_B V_G = e \int_0^\infty D(\epsilon) f(\epsilon, \mathcal{T}_e^1, \mu_e^1) d\epsilon - e \int_{-\infty}^0 D(\epsilon) [1 - f(\epsilon, \mathcal{T}_h^1, \mu_h^1)] d\epsilon \quad (9)$$

where  $f$  is the Fermi-Dirac distribution function,  $\mathcal{T}_{e/h}$  and  $\mu_{e/h}$  are the respective carrier temperatures and Fermi levels. The superscript 0 and 1 denotes the absence and presence of light excitation.  $D(\epsilon) = \frac{2}{\pi \hbar^2 v_f^2} \sqrt{\epsilon^2 + \epsilon_0^2}$  is the density-of-states, where  $\epsilon_0$  is introduced to account for the electron-hole puddles. Due to the photo-excitation, the carriers will be driven away from equilibrium, characterized by a non-equilibrium Fermi energy  $\mu_{e/h}^1$  and an elevated carrier temperatures  $\mathcal{T}_{e/h}^1$  compared to the ambient  $\mathcal{T}_{e/h}^0$ .



At steady state, electrons and holes are allowed to thermalize among themselves, i.e.  $\mathcal{T}_e = \mathcal{T}_h$  and  $\mu_e^1 = \mu_h^1$ , facilitated by femtosecond time scale carrier-carrier scattering processes [4, 5]. Here,  $\mathcal{T}_{e/h}^1$  can be described by  $\mathcal{T}_{e/h}^1 - \mathcal{T}_0 = \dot{Q}L/\kappa_0$  where  $\dot{Q}$  is the absorbed laser power,  $L$  the device length and  $\kappa_0$  is the electronic thermal conductivity. Since  $\sigma$  and  $\kappa_0$  are related through the Wiedemann-Franz relation,  $\mathcal{T}_{e/h}^1 - \mathcal{T}_0$  is then proportional to  $1/\mathcal{T}_0\sigma$ , where the proportionality constant is determined to give us  $n_{e/h}^* \approx 5 \times 10^{13} \text{ m}^{-2}$  at  $V_G = 0$ . This corresponds to  $\mathcal{T}_{e/h}^1 - \mathcal{T}_0 \approx 8 \text{ K}$  and  $12 \text{ K}$  at  $\mathcal{T}_0 = 300 \text{ K}$  and  $200 \text{ K}$  respectively. The photo-excited carriers  $n_{e/h}^*$  can then be numerically determined with Eq. 8-9 by imposing charge conservation  $n_e^* = n_h^*$ . Having calculated  $n_{e/h}^*$  as a function of  $V_G$  then provides us with an estimation of  $J_{PV}(V_G)$  used in the main manuscript.

In our analysis, we have extracted the photo-induced carrier density  $n^*$  from electrical measurements described above. Alternatively, one can also estimate the photo-induced carrier density based on our light excitation condition. However, uncertainty in various parameters render it less accurate than the electrical method. Nevertheless, we can perform estimates of the photo-induced carrier density based on our light excitation condition. In our experiments, the laser power is  $P = 370 \mu\text{W}$  with focal area  $a_{spot} = \frac{\pi}{4}(0.7)^2 \mu\text{m}^2$ . Light absorption at  $\lambda=690\text{nm}$  (i.e. photon energy  $E_{ph} = 1.8 \text{ eV}$ ) in graphene on  $90\text{nm SiO}_2$  is  $\alpha \approx 2.5\%$ . The photo-induced carrier density can be expressed as  $n_{e/h}^* = M\alpha P\tau_{rc}/E_{ph}a_{spot}$ , where  $M$  is the carrier multiplication factor and  $\tau_{rc}$  is the carrier recombination time. Since  $n_{e/h}^* \approx 5 \times 10^{13} \text{ m}^{-2}$ , we estimate that  $M\tau_{rc} \approx 0.6 \text{ ps}$ , which seems reasonable [6].

## VI. INTRINSIC ELECTRON-PHONON LATTICE HEATING

Electron-electron interaction results in an energy equilibration of the electronic system but does not lead to a net energy loss. The dominant energy loss pathways are due to phonons [3, 7–9]. In particular, electronic cooling in graphene due to intrinsic acoustic/optical phonon scattering processes has been well studied [7, 8]. For example, the electron-lattice energy transfer mediated by acoustic phonons has the following power density ( $\text{Wm}^{-2}$ ) given by [7],

$$Q_{ac} \approx \frac{D_{ac}^2 k_B}{\hbar \rho_m v_f^2} (\mathcal{T}_e - \mathcal{T}_L) \frac{1}{\pi} \int dk k^3 f(\epsilon_k, \mathcal{T}_e, \mu) \quad (10)$$

where  $D_{ac} \approx 20$  eV is the acoustic phonon deformation potential and  $\rho_m$  is mass density of graphene. For the experimental condition  $\mathcal{T}_e - \mathcal{T}_L \approx 10$  K and undoped graphene,  $Q_{ac}$  is only of the order of  $10^2$  Wm $^{-2}$ . Under some doping and temperature conditions, the optical power density  $Q_{op}$  may dominate over its acoustic counterpart [7], however  $Q_{op}/Q_{ac}$  is generally  $< 100$  over the range of experimentally relevant conditions.

- 
- [1] E. H. Nicollian and J. R. Brews, “Mos physics and technology,” *John Wiley and Sons*, 1982.
- [2] M. Cutler and N. F. Mott, “Observation of anderson localization in an electron gas,” *Phys. Rev.*, vol. 181, p. 1336, 1969.
- [3] J. C. W. Song, M. S. Rudner, C. M. Marcus, and L. S. Levitov, “Hot carrier transport and photocurrent response in graphene,” *Nano Lett. ASAP*, 2011.
- [4] R. Kim, V. Perebeinos, and P. Avouris, “Relaxation of optically excited carriers in graphene,” *Phys. Rev. B*, vol. 84, p. 075449, 2011.
- [5] M. Breusing, C. Ropers, and T. Elsaesser, “Ultrafast carrier dynamics in graphite,” *Phys. Rev. Lett.*, vol. 102, p. 086809, 2009.
- [6] P. A. George, J. Strait, J. Dawlaty, S. Shivaraman, M. Chandrashekhhar, F. Rana, and M. G. Spencer, “Ultrafast optical-pump terahertz-probe spectroscopy of the carrier relaxation and recombination dynamics in epitaxial graphene,” *Nano Lett.*, vol. 8, p. 4248, 2008.
- [7] R. Bistritzer and A. H. MacDonald, “Electronic cooling in graphene,” *Phys. Rev. Lett.*, vol. 102, p. 206410, 2009.
- [8] W. K. Tse and S. D. Sarma, “Energy relaxation of hot dirac fermions in graphene,” *Phys. Rev. B*, vol. 79, p. 235406, 2009.
- [9] S. V. Rotkin, V. Perebeinos, A. G. Petrov, and P. Avouris, “An essential mechanism of heat dissipation in carbon nanotube electronics,” *Nano Lett.*, vol. 9, p. 1850, 2009.

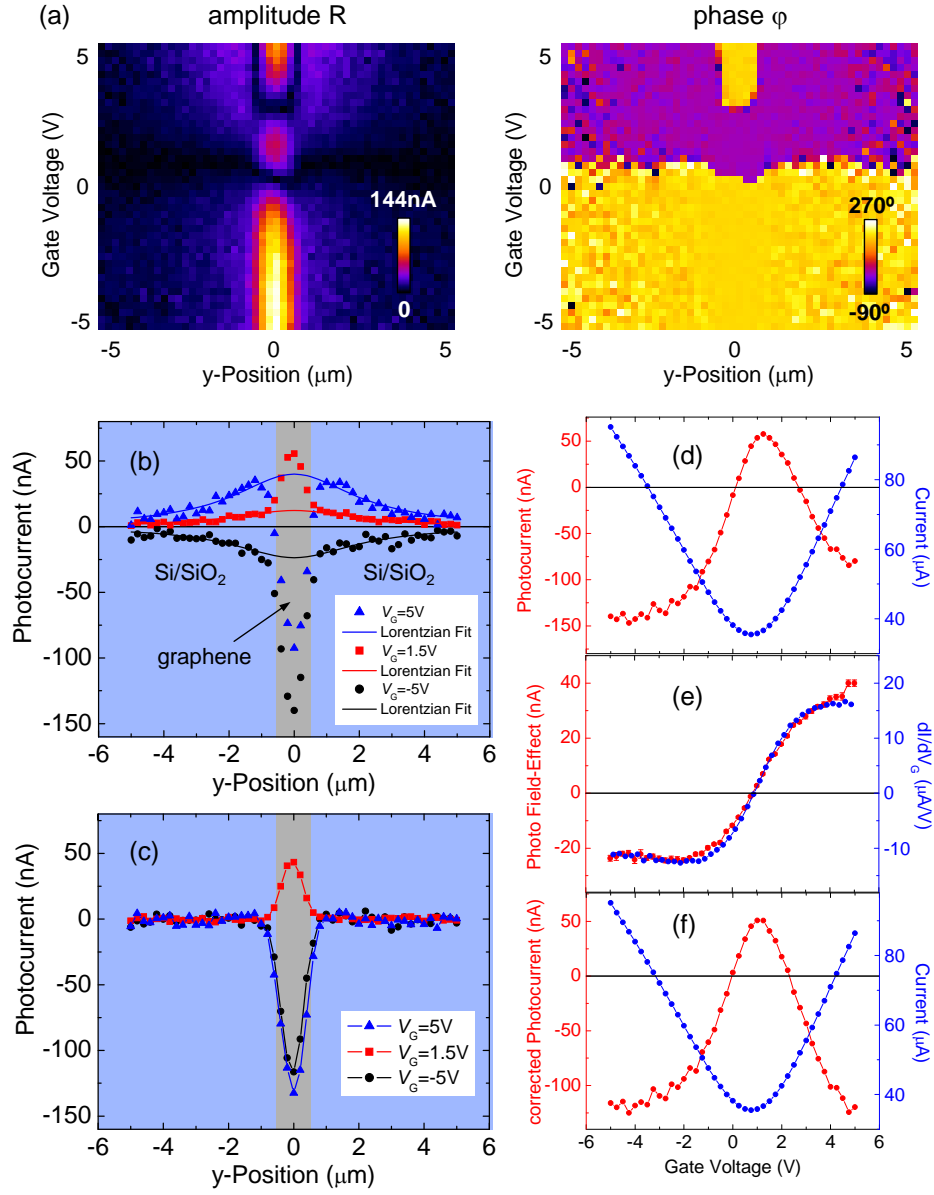


FIG. 1: **(supplemental) Correction for the Photo Field-Effect.** (a) Photocurrent amplitude and phase as a function of  $y$ -position (perpendicular to the graphene device) and gate voltage. (b) Fitting of the photo field-effect component of the photocurrent to Lorentzians for selected gate voltages. The gray-shaded area indicates the position of the  $1\mu\text{m}$  wide graphene device, which was excluded for fitting purposes. (c) Photocurrent as a function of  $y$ -position corrected for the photo field-effect for the same gate voltages as in (b). (d) Measured AC photocurrent (red) in the center of the graphene FET in Fig. 2 of the main text, and corresponding DC current (blue) as a function of gate voltage. (e) Photo field-effect at the center of the graphene channel (red) extracted from fits similar to the ones in (b). The photo field-effect is proportional to the transconductance (blue). (f) Photocurrent (red) corrected for the photo field-effect. The DC current (blue) is plotted again as a reference.

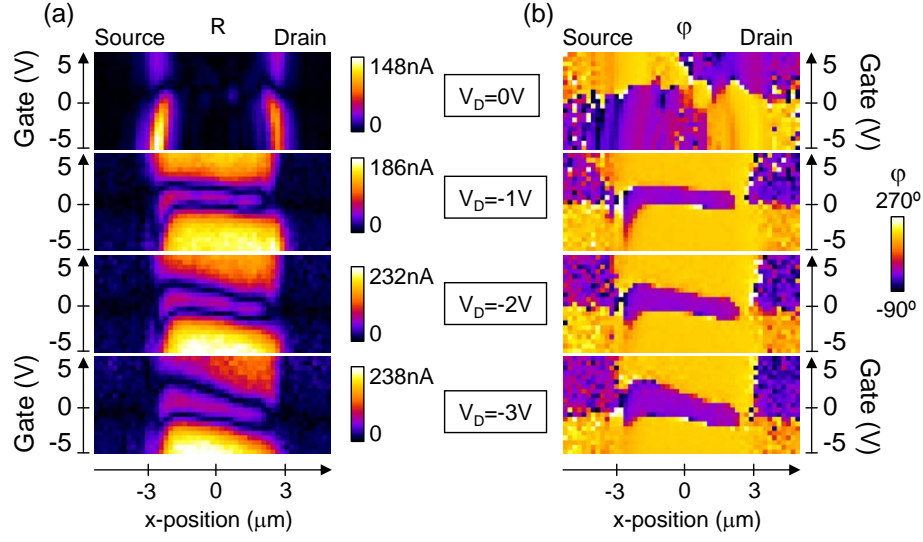


FIG. 2: (supplemental) Spatial behavior of the AC photocurrent at low and high drain bias. Amplitude (a) and phase (b) of the AC photocurrent as a function of gate voltage and x-position along the graphene device for drain voltages from  $V_D = 0\text{V}$  to  $-3\text{V}$ .